Mast Bumping Simulation and Mitigation Analysis for Teetering Rotor Systems

Ananth Sridharan
Assistant Research Scientist

Inderjit Chopra
Distinguished University Professor

Alfred Gessow Rotorcraft Center, Department of Aerospace Engineering
University of Maryland, College Park, MD, USA

Stephen Turnour
Aerospace Engineer and Certification Manager
Robinson Helicopter Company, Torrance, CA, USA

Abstract

This paper presents modeling and simulation, and validation of a teetering rotor helicopter using rotorcraft comprehensive analysis. Multibody kinematics with rotating reference frames is used to model the Robinson tri-hinge type teetering hub, and the associated rotor-body couplings for the R66 helicopter. A kinematic analysis of the swashplate is carried out to identify the unique dual delta-3 coupling for this platform, as well as the mapping from pilot controls to swashplate and subsequently to blade pitch control inputs. This model is partially validated with test data for two level flight speed sweeps for different CG locations within the fuselage. Finally, the effect of weight/CG location, steady pilot cyclic controls and time-varying stick inputs are studied to identify combinations of flight conditions and controls that may reduce safety margins for mast bumping, i.e. when the teeter system contacts the rotor shaft. Increasing the horizontal tail mounting angle on the fuselage may reduce the teeter angles in cruise, at the possibly prohibitive cost of reduced static longitudinal stability.

NOMENCLATURE

$b_{1c}, b_{1s}, ..$	Fourier coefficients of teeter angle, rad
B_o	Average flap angle at coning hinge, rad
B_d	Differential flap angle at coning hinge, rad
CG	Center of Gravity
e_x	Spanwise offset of coning hinge, ft
e_z	Vertical underslung offset of coning hinge, ft
FSCG	Fuselage Station for vehicle CG, inch
$\mathrm{I_b}$	Blade flap inertia about teeter hinge, slug-ft^2
I_β	Blade flap inertia about coning hinge, slug-ft^2
$\mathrm{K}_{P_{\beta_\mathrm{T}}}$	Delta-3 coupling constant from teeter
$\mathrm{K}_{P_{\beta_o}}$	Delta-3 coupling constant from coning
$\mathrm{M_b}$	Blade mass, slugs
M_{teeter}	Flap bending moment at teeter hinge, ft-lb
$\mathrm{M_{T1}}$	Moment at teeter hinge from blade 1, ft-lb
$\mathrm{M_{T2}}$	Moment at teeter hinge from blade 2, ft-lb
$\mathrm{N_h}$	Number of blade mode and teeter harmonics
$\hat{\boldsymbol{i}}, \hat{\boldsymbol{j}}, \hat{\boldsymbol{k}}$	Unit vectors of coordinate system
$w(x,t)$	Total flap deflection of rotor blade, ft
$w_e(x,t)$	Blade flap deflection relative to coning hinge, ft
β_T	Teeter angle, radians
β_o	Angle at blade coning hinge, radians
β_1	Angle at blade 1 coning hinge, radians
β_2	Angle at blade 2 coning hinge, radians
$\delta_o, \delta_{\mathrm{lat}}, \delta_{\mathrm{lon}}$	Pilot controls
$\Delta\psi$	Swashplate phase angle
λ	Rotor inflow ratio
ν_β	Non-dimensional flap frequency
ν_T	Non-dimensional teeter frequency
Ω	Rotor speed, rad/s
ψ	Blade azimuth, rad
θ	Blade root pitch angle, radians
θ_{con}	Blade pitch angle due to pilot inputs, rad
$\theta_0, \theta_{1c}, \theta_{1s}$	Swashplate collective and cyclic inputs, rad

INTRODUCTION AND MOTIVATION

The use of a simple two-bladed main rotor in helicopter designs for commercial aviation with relatively modest payload (1 – 6 passengers) is an effective approach to minimizing acquisition and maintenance costs. The teetering rotor system is a relatively lightweight choice for a two-bladed rotor: the rotor mast and support structure weight is reduced because flap bending moments from the individual blade are not transmitted into the mast. Examples of teetering-rotor helicopters include the Robinson R22, R44 and R66, and the Bell 206, UH-1H "Huey", and AH-1 "Cobra". Teetering designs can be subdivided into two classes: the "Bell-type" design, in which the blades are cantilevered to each other, or the "Robinson-type" design, where each blade has its own flapping hinge in addition to the teetering hinge.

These two teetering rotor designs are shown in Figs. 1 and 2 for the R22 and AH-1, respectively. Most teetering rotor systems also feature an underslung configuration, where the root of the blade is vertically offset below the teeter hinge. The rotor system is designed so that with blades coned at their normal operating angle (pre-cone angle for Bell-type rotors or normal operating angle for Robinson-type rotors) the blade's spanwise center of gravity rotates in a plane containing the

Fig. 1. R22 "tri-hinge" hub

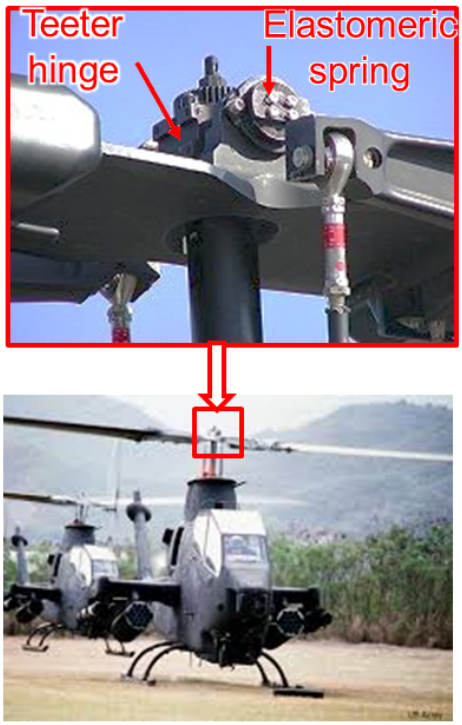

Fig. 2. AH-1 Cobra teetering hub

teeter hinge. This design reduces in-plane Coriolis forces. In this work, we consider the Robinson-type rotor system with the "tri-hinge" hub. For this system, cyclic flapping is driven by teetering motion rather than individual blade flapping.

If one blade produces more lift than the other, then the lift imbalance causes the entire assembly to teeter, i.e., the blade with more lift flaps up and the blade with lower lift flaps down relative to the mast.

A disadvantage of a teetering rotor design, a consequence of the lack of flapwise moments at the mast, is the low control moment when the rotor is lightly loaded (e.g. during a low-g maneuver). When the rotor is lightly loaded, low control effectiveness can lead to the pilot applying large control inputs, which in turn can lead to excessive blade teetering. Excessive flapping can lead to contact between the rotor hub and mast. This phenomenon is called "mast bumping" and often leads to catastrophic failure of the mast or blade contact with the fuselage. Currently, it is addressed by training pilots to avoid a lightly loaded rotor.

PREVIOUS WORK

One of the earliest works on teetering rotor dynamics modeling was performed by Shamie and Friedmann (Ref. 1). The governing structural dynamics for teetering blade dynamics were derived and the aeroelastic system was used to perform stability analysis. Yeo and Chopra (Ref. 2) also modeled the AH-1 Cobra's teetering rotor using UMARC (a rotorcraft comprehensive analysis) coupled to a free-vortex wake model. The comprehensive analysis/free wake model was coupled to a flexible airframe model to study the qualitative and quantitative accuracy of predicted vibration in the airframe. Another work on teetering rotor stability analysis was performed by Floros and Johnson (Ref. 3) using the rotorcraft comprehensive analysis CAMRAD-II. The teetering configuration was found to be aeroelastically stable under steady flight conditions up to an advance ratio of μ=3.0 when applied to a slowed-rotor compound helicopter.

Rezgui et al. (Ref. 4) also considered a teetering rotor for an autogyro, and presented comparison of simulation results and experimental data for a scaled model. The rotor was modeled as a teetering rigid structure with one degree of freedom. In their study, a lightly loaded rotor was observed to exhibit reduced aeroelastic stability margin in forward flight; this observation is (co-incidentally) consistent with the guidelines given to pilots, i.e., to avoid flying with lightly loaded rotors in teetering rotor helicopters. The dynamic behavior of a two-bladed gimbaled rotor was assessed by Avanzini et al. (Ref. 5) using a simulation model. Their modeling consisted of rigid rotor blades, linear airfoil behavior and uniform quasi-static inflow. Their study used elastomeric springs at the teeter hinge to retain control effectiveness in zero-g flight. In related work, Shen et al. (Ref. 6) used a multibody dynamics formulation using the research code MBDyn to model a teetering hub for a tilt-rotor helicopter. The study used very detailed numerical modeling of the coupled flap-lag-torsion blade dynamics.

Though many of these studies modeled the teetering rotor boundary condition with great precision, mast bumping onset and identification was not addressed directly in most studies. Drees (Ref. 7) filed a patent for isolating 2/rev hub spring moment vibrations while providing control power during zero-g flight. Studies carried out by Bell Helicopter (Ref. 8) also

highlighted that a hub spring could be beneficial in reducing flapping at all flight conditions, but have detrimental consequences for rotor system fatigue lives, vibration isolation, and possibly rotor stability. A simulation study was performed for a teetering rotor helicopter by varying various combinations of rotor thrust, advance ratio, swashplate step inputs and vehicle center of gravity by Dooley (Ref. 9). At low or negative-g flight and CG at the allowable extremes, or with abrupt control inputs, blade flapping was found to exceed acceptable limits. A study by Sarathy et al. (Ref. 10) used FLIGHTLAB to simulate the dynamics of the R22 helicopter. The rotor was modeled using rigid blades, quasi-steady airfoil tables and a dynamic inflow model. Speed and thrust sweeps for steady-state analysis, as well as transient analysis using abrupt pilot inputs, were presented to demonstrate the onset of mast bumping.

Though there are several studies focusing on the individual components of a teetering rotor helicopter, there does not appear to be any systematic design sensitivity study on mast bumping in open literature, which is the intent of this paper. **The objective of this work** is to identify the rotor parameters and critical combinations of flight condition and blade loading that triggers mast bumping, and investigate approaches to mitigating this phenomenon through design.

METHODOLOGY

Comprehensive Analysis

A comprehensive rotorcraft analysis was developed in-house at the University of Maryland's Alfred Gessow Rotorcraft Center (Ref. 11) by the authors in a previous work. This analysis is used as a basis for the present study to model the vehicle flight dynamics and rotor aeromechanics. The airframe and the horizontal and vertical stabilizers are modeled as rigid bodies with table-lookup aerodynamics. Rotor-body couplings are modeled using multibody-type rotations with exact kinematics. Rotor blades are modeled as geometrically exact Euler-Bernoulli beams with flap, lag and torsion dynamics. Modal reduction may be optionally applied to the finite element formulation of the rotating blade dynamics and reduce the size of the system being analyzed while preserving the dominant blade motions. Tail rotor loads are computed using a disc model with uniform dynamic inflow. The Maryland Free-vortex Wake model (Ref 12) is coupled to the aero/flight mechanics solver to compute the rotor inflow. The Peters-He dynamic inflow model (Ref 13) is also integrated into the analysis, and is available for use in place of the free wake model. This simulation has been validated for single and multi-rotor configurations, and was recently used for CFD-CSD analysis of coaxial rotorcraft (Ref 14). For time marching, an implicit dual-step integrator is implemented based on the work in Ref 15. The analysis also features a harmonic balance based coupled trim process that simultaneously obtains the blade motions, vehicle orientations and pilot controls in non-accelerating (steady) flight conditions.

The baseline analysis was originally formulated for articulated and hingeless rotors. In this work, the model is expanded to accommodate a teetering rotor system as described below.

Tri-hinge Model

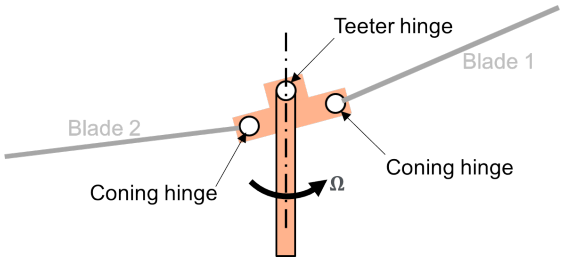

Fig. 3. Tri-hinge layout

The tri-hinge assembly is shown in Fig. 3. It consists of a central teeter beam attached to the rotor shaft through a teeter hinge. The teeter hinge does not transmit flap bending moments to the rotor mast, but does transmit all other loads, i.e. centrifugal, vertical and lateral shears and blade torque. The pitching moments are carried to the airframe through the pitch links. The teeter beam also features two individual blade flap hinges offset vertically below and outboard of the teeter hinge. In Robinson notation, the individual blade flap hinges are called "coning hinges", owing to the fact that blade flap angles are nominally constant at these hinges and all cyclic flapping occurs due to blade teetering in steady flight (Appendix A). The relevant hinge offsets e_x and e_z are shown in Fig. 4. The teeter angle β_T is defined to be positive when blade 1 moves up due to teeter motion and blade 2 moves down.

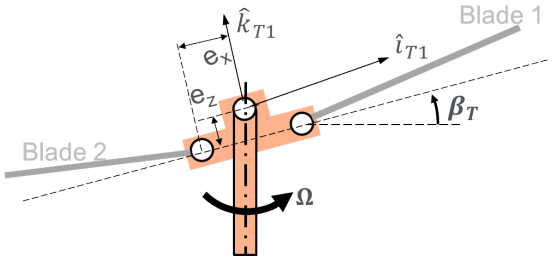

Fig. 4. Tri-hinge parameters and blade 1 teeter frame

Two additional reference frames are introduced into the analysis, one for each blade. This frame is referred to as the blade teeter frame. The blade teeter frame is obtained from the rotating shaft reference frame through a rotation about the Y-axis (lead-lag direction). Blade 1 is chosen as the reference blade, and is indicated in Figs. 3 and 4.

The blade 1 teeter reference is obtained through a rotation -β_T about the shaft Y-axis, and is given by

$$\begin{Bmatrix} \hat{\imath} \\ \hat{\jmath} \\ \hat{k} \end{Bmatrix}_{T1} = \begin{bmatrix} \cos\beta_T & 0 & \sin\beta_T \\ 0 & 1 & 0 \\ -\sin\beta_T & 0 & \cos\beta_T \end{bmatrix} \begin{Bmatrix} \hat{\imath} \\ \hat{\jmath} \\ \hat{k} \end{Bmatrix}_{S1} \quad (1)$$

The blade 2 teeter reference is obtained through a rotation

β_T about the shaft Y-axis, and is given by

$$\begin{Bmatrix} \hat{i} \\ \hat{j} \\ \hat{k} \end{Bmatrix}_{T2} = \begin{bmatrix} \cos\beta_T & 0 & -\sin\beta_T \\ 0 & 1 & 0 \\ \sin\beta_T & 0 & \cos\beta_T \end{bmatrix} \begin{Bmatrix} \hat{i} \\ \hat{j} \\ \hat{k} \end{Bmatrix}_{S2} \quad (2)$$

Here, T1 refers to the teeter reference frame for blade 1, while T2 refers to the teeter reference frame for blade 2 and S1, S2 represent the rotating blade (undeformed) reference frame when the teeter angle is zero.

The origin for the blade teeter reference frames is at the teeter hinge. Therefore, the origin of the individual blade coordinate system does not change with the teeter angle β_T. Blade positions are tracked with respect to the origin of the blade teeter frame for each blade. The elastic deflections with respect to the underformed blade positions are superposed on the underslung hinge offsets e_z, i.e.

$$w(x,t) = w_e(x,t) - e_z \quad (3)$$
$$\dot{w}(x,t) = \dot{w}_e(x,t) \quad (4)$$
$$\ddot{w}(x,t) = \ddot{w}_e(x,t) \quad (5)$$

Here, w_e refers to the elastic flap deflection (including vertical deflection due to individual blade flap motions) and w is the total flap deflection. The lag deflections are purely due to elastic bending. Axial motions due to the vertical offset between the teeter hinge and blade flap hinges are accounted for through translation of coordinates described earlier. Elastic twist of the rotor blade sections are also modeled, but the modeling is not modified for this rotor system.

Pitch-flap coupling: delta-3

The tri-hinge model features a unique feedback system for blade pitch angles based on flapping. The top of the pitch link lies ahead of the blade pitching axis, while the spanwise location of the pitch link is between the teeter hinge axis and the blade flap hinge axis. Therefore, when the blade assembly teeters about the central hinge, a stabilizing delta-3 feedback is imposed on blade pitch motions (flap up motion causes a nose-down pitch angle). However, if the blade angle increases at the outboard hinge (coning hinge), the resulting pitch motions are destabilizing, i.e. pitch up motion for increase in coning angles.

The final blade rotations about the pitch bearing are a result of both imposed control from the pilot stick motions (swashplate motions), as well as feedback from the kinematics of the pitch link. Though the original kinematics of delta-3 feedback are strictly nonlinear, a very good linear approximation was obtained (Appendix B) which agrees well with trigonometry-based approximations linearized about zero blade motions.

The root pitch angles for blades 1 and 2 are given by

$$\theta_1 = \theta_{con1} - 0.332\beta_T + 0.23\beta_1 \quad (6)$$
$$\theta_2 = \theta_{con2} + 0.332\beta_T + 0.23\beta_2 \quad (7)$$

Here, the first term θ_{con} refers to the imposed control from motion of the pilot stick. The second term reflects the stabilizing delta-3 feedback from teeter motions β_T. The equivalent delta-3 angle is $\tan^{-1}(-0.332)$ = -18.37 deg for teetering. The final term represents the destabilizing feedback arising from blade rotations at the coning hinges, i.e. β_1 and β_2 for blades 1 and 2 respectively. The equivalent delta-3 angle is +12.93 deg for coning motions. The negative sign in the teeter angle term for the second blade reflects the fact that when blade 1 moves up, blade 2 moves down when the teeter beam pivots about the teeter hinge.

Main Rotor Controls

The kinematics of the swashplate and pitch links are such that when cyclic inputs are applied by the pilot stick, the corresponding blade pitch angles have a swashplate phase lag $\Delta\psi$. The resulting root pitch angles of the main rotor blades is given by

$$\theta_{con}(\psi) = \theta_o + \theta_{1c}\cos(\psi - \Delta\psi) + \theta_{1s}\sin(\psi - \Delta\psi)$$

Rotor Loads and Teeter Dynamics

Rotor aerodynamic loads are calculated based on the local sectional angles of attack and dynamic pressure using Mach-tabulated NACA 0012 airfoil properties. The sectional velocities include the effect of blade teetering motions and the tri-hinge layout. Similarly, inertial loads experienced by the rotor blade cross-sections are computed from the total accelerations and velocities, including the effect of teetering motions. These distributed loads are used with the blade mode shapes to compute the modal forcing for the blades. The components of total force and moment acting at the teeter hinge are summed using numerical quadrature. The contribution to "hub" moment from each blade at the teeter hinge is obtained in a manner identical to articulated rotor configurations. The total flap moment at the teeter hinge is given by

$$M_{teeter} = M_{T1} - M_{T2}$$

M_{T1} and M_{T2} are the flap bending moments at the teeter hinge (origin of blade undeformed rotating reference frame) due to aerodynamic and inertial loads on blades 1 and 2, respectively. Due to the second blade being diametrically opposite to the first blade, a negative sign to M_{T2} is applied to calculate the total moment at the teeter hinge in the rotating undeformed axis of blade 1.

At the teeter hinge, the flap bending moment must vanish (boundary condition). Therefore, the governing equation corresponding to the teeter degree of freedom β_T is

$$M_{T1} - M_{T2} = 0 \quad (8)$$

Trim for Teetering Rotors

A numerical Galerkin method is used to obtained the steady-state rotor response and perform propulsive trim in the baseline analysis. The spanwise distribution of rotor loads are

sampled over one rotor revolution and used to calculate (in sequence) the residuals of the rotor modal equations, rotor hub loads and residuals of the vehicle rigid-body Newton-Euler equations of equilibrium.

For a teetering rotor, the additional degree of freedom β_T introduces a corresponding governing equation given by Eqn. 8. To include this degree of freedom into the trim process, additional trim variables and a corresponding number of trim equations are required.

Given that the baseline analysis uses harmonic balance to resolve rotor blade motions over one revolution, the natural choice for teeter trim variables is the Fourier coefficients of the teeter angle β_T. Therefore, the variation of the teeter angle over one revolution in trimmed flight is assumed to be

$$\beta_T(\psi) = \sum_{i=1}^{N_h} b_{ic}\cos i\psi + b_{is}\sin i\psi \qquad (9)$$

The baseline trim process is augmented with additional trim variables: the Fourier coefficients of the teeter hinge moment $(b_o, b_{1c}, b_{1s}, b_{2c}, b_{2s}, ...)$. The corresponding trim residuals are the Fourier coefficients of the teeter hinge moment sampled over one rotor revolution. The additional trim equations for the teeter hinge are given by

$$\begin{aligned} 0 &= \int_0^{2\pi} M_{\text{teeter}}\cos\psi d\psi \\ 0 &= \int_0^{2\pi} M_{\text{teeter}}\sin\psi d\psi \\ 0 &= \int_0^{2\pi} M_{\text{teeter}}\cos 2\psi d\psi \\ 0 &= \int_0^{2\pi} M_{\text{teeter}}\sin 2\psi d\psi \\ &... \end{aligned}$$

Model Description

A simulation model of the R66 was created in the comprehensive analysis. The vehicle and rotor properties are given in Table 1. The mapping from pilot stick motions to swashplate motions, and from swashplate motions to actual blade collective and cyclic pitch inputs are each considered linear.

Description of Flight Test Data

Flight tests were carried out with an R66 helicopter using instrumentation on one main rotor blade. The quantities measured include

1. Blade flap and lag bending loads
2. Pitch link loads
3. Main rotor and tail rotor torque
4. Engine power output
5. Pilot collective and cyclic stick positions
6. Fuselage pitch and roll attitudes
7. Main rotor teeter and coning angles
8. Weight and CG stations (measured on ground)
9. Pressure altitude, airspeed and sink rate
10. Main rotor speed

The flight conditions tested are listed below:

1. Steady hover
2. Steady level flight
3. Steady left turn, 30 and 45 deg bank angle
4. Steady right turn, 30 and 45 deg bank angle
5. Steady climb
6. Autorotation

Four weight and CG combinations were flown at various airspeeds (up to 120 knots) and altitudes (3000 ft, 8000 ft, 12000 ft)

1. FSCG 8 inches ahead of MR, 2700 lb
2. FSCG 2 inches ahead of MR, 2700 lb
3. FSCG 9 inches ahead of MR, 2200 lb
4. FSCG 2.5 inches behind MR, 2300 lb

Apart from the factorial sweep of forward flight speeds, altitudes, left/right turns and weight/CG combinations, other flight conditions were also examined, where the tail rotor torque was not measured, but blade motions were tracked. As teeter angles are the relevant quantities to track for mast bumping, flight tests that record blade teeter angles are focused on.

For each flight condition, data was recorded during a sampling window of a few rotor revolutions (3 to 4). The pitch and roll attitudes were obtained from the autopilot, and the minimum and maximum values recorded in the sampling window are both shown as data points for a given airspeed. Overall, the difference between the upper bound and mean value for body pitch and roll attitudes is less than 1 degree.

The teeter and coning angles time histories were also found to vary across rotor revolutions. The blade motion data was broken down into steady and 1/rev components, and the variation of these Fourier coefficients across the sampling window is also calculated. The upper and lower bounds of these values are shown to quantify the scatter in the test data. Generally, the difference between the mean value and the upper bound of the data is less than 0.5 deg for the coning angles, and less than 0.25 deg for the teeter angles.

Table 1. Vehicle parameters

Parameter	Value
Gross weight	2200 – 2700 lb
FSCG range	91 inch to 102.5 inch
Equivalent flat-plate area	4.75 ft^2
Main rotor properties	
Radius R	16.5 ft
Number of blades, N_b	2
Geometric solidity σ_{MR}	0.0371
Tip speed V_{TIP}	705 ft/s
Blade twist	- 4 deg (linear)
Airfoil (model)	NACA 0012
Delta-3 angle (teeter)	-18.4 deg (stabilizing)
Delta-3 angle (coning)	+12.95 deg (destabilizing)
Fuselage station	100 inch
Vertical offset from CG	43 inch (nominal)
Shaft tilt	0 deg
Swashplate phase lag $\Delta\psi$	18 deg
Pilot controls	**Swashplate inputs**
Collective δ_o = 0%	θ_o = 0.5 deg
Collective δ_o = 100%	θ_o = 13.5 deg
Lateral cyclic δ_{lat} = 0%	θ_{1c} = + 8.0 deg
Lateral cyclic δ_{lat} = 100%	θ_{1c} = - 6.5 deg
Longitudinal cyclic δ_{lon} = 0%	θ_{1s} = -13.9 deg
Longitudinal cyclic δ_{lon} = 100%	θ_{1s} = +13.9 deg
Tail rotor properties	
Radius R	2.5 ft
Number of blades, N_b	2
Geometric solidity σ_{MR}	0.1167
Tip speed V_{TIP}	635 ft/s
Blade twist	0 deg (untwisted)
Empennage	
Horizontal tail area	4.67 ft^2
Vertical tail area	6.86 ft^2
Distance: HT to MR hub	227 inch
Distance: VT to MR hub	231 inch

RESULTS

Blade natural frequencies were extracted using a modified modal analysis for the teetering configuration with degrees of freedom for two blades and the teeter degree of freedom. The fan plot for the R66 blade is shown in Fig. 5, and the teetering mode frequencies are compared to the modes for an articulated blade. For a teetering rotor, every odd mode corresponds to a combination of motions in which rotation of the teeter beam about the teeter hinge occurs, resulting in antisymmetric motion for blades 1 and 2 (marked "A" for antisymmetric). Every even mode corresponds to the teeter hinge being locked, i.e., identical to an articulated rotor (with flap hinge offset). These modes are marked as "S" for symmetric, i.e., blades 1 and 2 have identical mode shape components. The flap, lag and torsion components for the first 3 symmetric and antisymmetric blade modes are given in Appendix C.

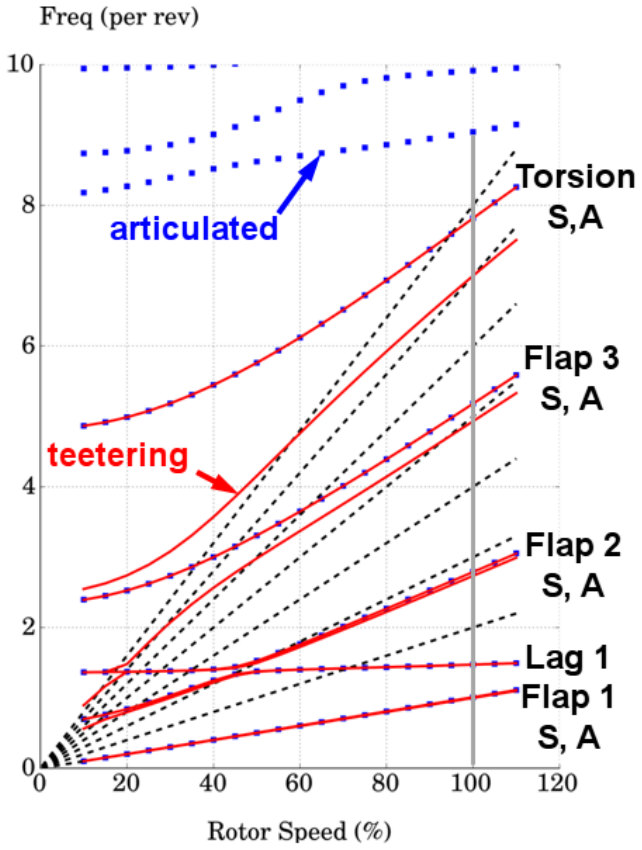

Fig. 5. Fan plot for elastic teetering rotor model; S for symmetric, A for Antisymmetric modes

Tail Rotor Drag Coefficient

In cruise, the tail rotor is off-loaded by the vertical fin, and the rotor torque is nominally constant with airspeed. Though the simulation predictions reflect this trend as shown in Fig. 6, the tail rotor torque in cruise is largely a function of the zero-lift drag coefficient. This parameter was tuned based on measured tail rotor torque to achieve the good agreement shown in Fig. 6. The derived model for tail rotor section drag coefficient is

$$C_{d_{TR}} = 0.017 + 0.65\alpha^2$$

In the following section, predictions from the simulation model are compared against two flight tests: Flight 423, and

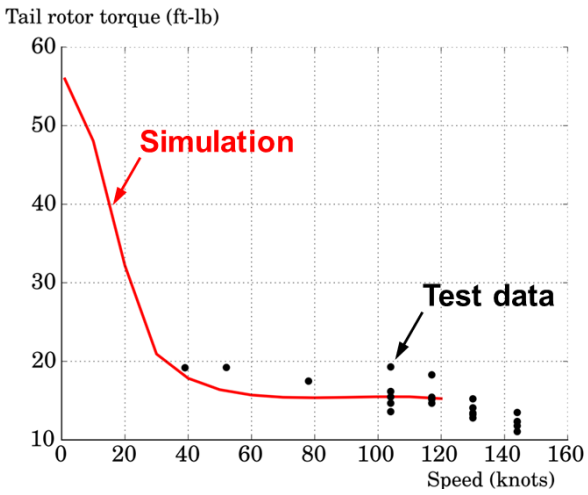

Fig. 6. Tail rotor torque: predictions vs. test data

Flight 429, in which trim conditions were recorded over a range of airspeeds. The details of the two flight tests are given in Table 2.

Table 2. Test flight conditions

Parameter	**Flight 439**	**Flight 423**
Weight	2200 lb	2200 lb
FSCG	91 inch	102.5 inch
BLCG	-1 inch	0.16 inch
Altitude	4300 ft	3696 ft

Comparison to test data: Flight 439

Figure 7 shows the comparison of main rotor power required to fly in steady forward flight vs. test data over a range of airspeeds at the specified altitude. Generally, predictions of main rotor power follow the trends well. However, even a 25 hp difference for this vehicle at 80 knots corresponds to 20% error (relative to 125 hp).

Figure 8 shows the comparison of main rotor controls (collective and two cyclics) with test data. Generally, collective predictions follows the expected trend of initial reduction followed by increase with airspeed beyond 60 knots. The longitudinal control input θ_{1s} is driven by the need to tilt the tip-path-plane forwards to overcome increasing vehicle drag with airspeed. The lateral control input θ_{1c} remains nominally constant with airspeed. This behavior, though expected, is the result of the unique swashplate kinematics specific to the R66.

The arrangement of the pitch links on the swashplate is such that the blade pitch angles lag the corresponding swashplate movement by 108 deg. For example, if the swashplate purely tilts forward (moves up over the tail), then maximum blade pitch is achieved at 108 deg of azimuth. If this effect is not accounted for correctly, predictions of the lateral control

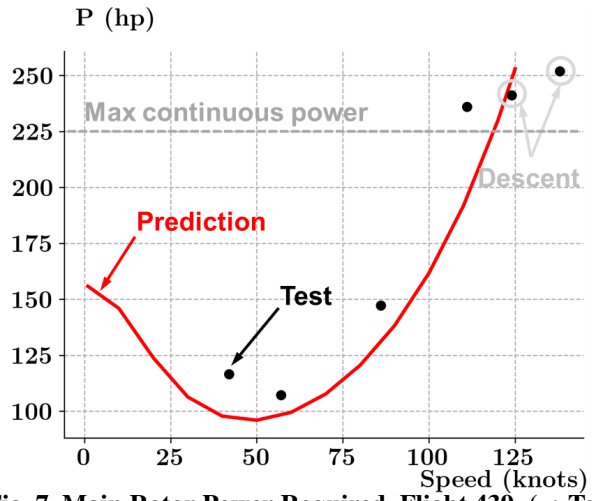

Fig. 7. Main Rotor Power Required, Flight 439. (•: Test)

input are polluted by some cross-coupling with the longitudinal control input and data correlation with test becomes poor. Therefore, accounting for the swashplate phase lag correctly is critical for accurate prediction of the lateral control input.

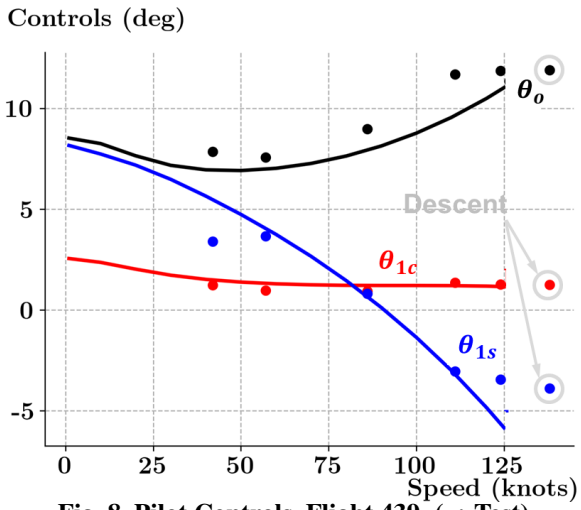

Fig. 8. Pilot Controls, Flight 439. (•: Test)

Figure 9 shows the comparison of body pitch and roll attitudes with the corresponding data sets for Flight 439. Generally, roll attitudes are very well predicted, and pitch attitudes trends and magnitudes are similarly well captured by the simulation. Towards the higher airspeeds ($\geq$ 120 knots), it was noted in the flight test that the pilot initiated a descent to avoid engine power draw exceeding the maximum continuous rating of 225 hp. Thus, the last two data points in this set are not level flights, but rather cases of shallow descent.

Figure 10 shows the variation of the 1/rev lateral and longitudinal components of the teeter angles with airspeed, and the corresponding flight test data. The "1s" component in blue is indicative of the lateral tip-path-plane tilt due to teetering motion, and both magnitudes and trends are very well predicted. Similarly, the longitudinal tip-path-plane tilt (1c component) captures the general behavior well, except at the highest airspeeds (descent cases in actual test). At 50 knots, the longitudinal tilt is relatively insensitive to airspeed, though

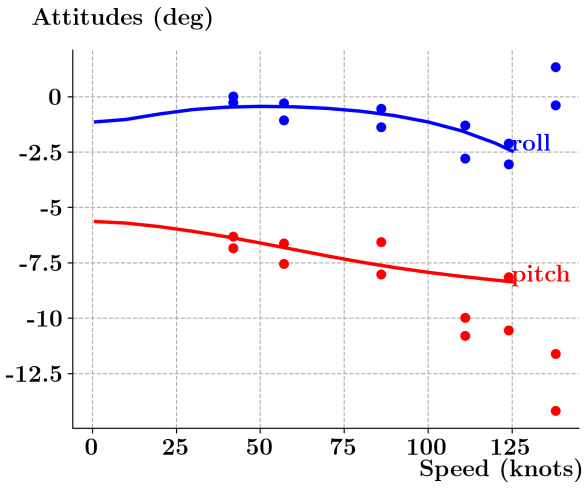

Fig. 9. Body Attitudes, Flight 439. (•: Test)

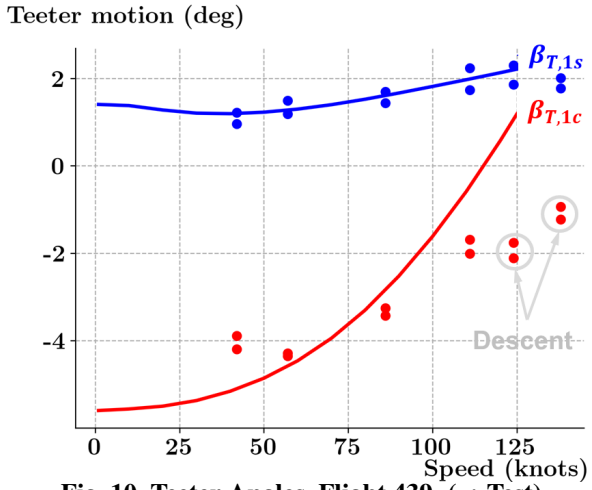

Fig. 10. Teeter Angles, Flight 439. (•: Test)

the simulations show a constant slope with airspeed typical of helicopters. The discrepancy may arise from the lack of modeling for wake impingement on the horizontal tail.

Figure 11 shows the variation of the steady, 1/rev cosine and 1/rev sine blade coning angles with airspeed. The steady coning angle exhibits an offset relative to the test data, while the lateral/longitudinal tip-path-plane tilts from coning are minuscule (less than 0.5 deg). The agreement with trends in the test data is not as good as the correlation observed for the control angles or body attitudes. Possible reasons for the discrepancy in mean coning angle may lie in the dissimilarity of magnitudes observed for the instrumented and non-instrumented blade. Another reason may be the exclusion of the flexible blade modes in the simulation model. To verify whether blade flexibility affects the coning angle predictions, additional simulations were conducted with the flexible modes included.

When the flexible modes are included, the predictions of rotor power, vehicle pitch attitudes, and teeter motions remain unchanged. However, the coning angle predictions are significantly altered, as shown in Fig. 12. The mean coning angle (flap angle at blade root) exhibits a near-constant behavior with airspeed, while the 1c and 1s components of the root

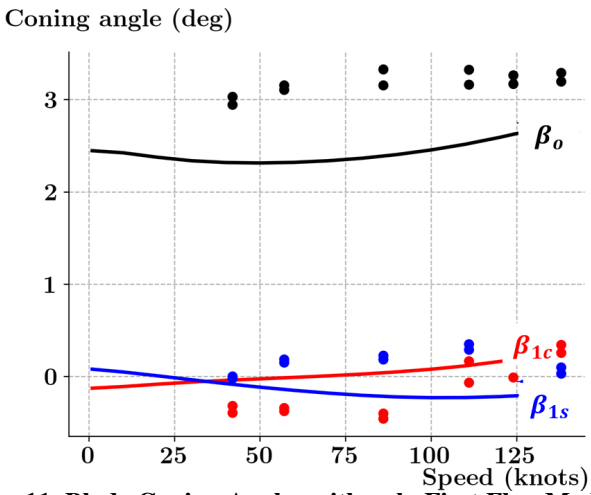

Fig. 11. Blade Coning Angles with only First Flap Modes, Flight 439. (•: Test)

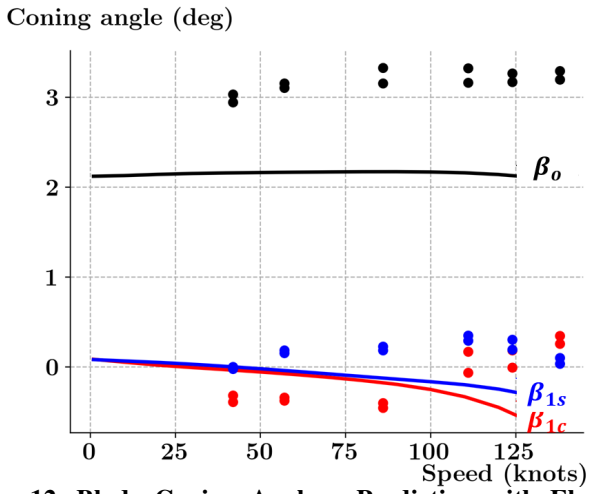

Fig. 12. Blade Coning Angles: Prediction with Elastic Modes, Flight 439. (•: Test)

flap angle decrease monotonically with airspeed. The agreement with test data does not improve, but this study shows the importance of including blade flexibility effects in comparing coning angle predictions to test data.

Comparison to test data: Flight 423

Figure 13 shows the variation of main rotor power required with airspeed at 3700 ft for Flight 423. Overall, agreement with test data is good for this case, though the test data indicates that two cases above 125 knots exceed the maximum continuous power rating. Strictly, engine power required must be used to compare against the maximum continuous power rating. However, in forward flight, the power required for accessories and tail rotor together constitute approximately 6.5 hp. At speeds approaching 120 knots, 6.5 hp is small enough compared to main rotor power required that it can be ignored.

Figure 14 shows the predicted and measured main rotor controls at various airspeeds for Flight 423. Collective pitch predictions are quite good, with a small under-prediction at higher speeds. The lateral control (red line) matches very well

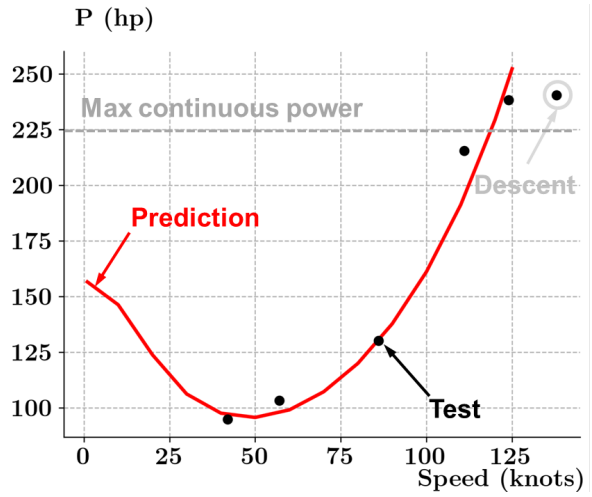

Fig. 13. Main Rotor Power Required, Flight 423. (•: Test)

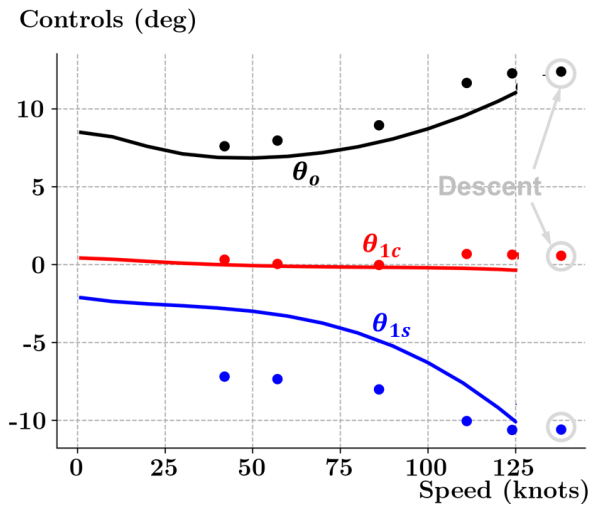

Fig. 14. Pilot Controls, Flight 423. (•: Test)

with test data, while the longitudinal input exhibits some offset relative to the test data. Based on Fig. 13, the last two test data points correspond to shallow descent to limit the engine power draw.

Figure 15 shows the comparison of predicted pitch and roll attitude at various airspeeds against measured body attitudes in cruise. Pitch attitude data shows approximately 1 deg of under-prediction throughout, while roll attitude shows 2 deg of excessive bank left compared to the test data. An analysis of the data reveals that the flight condition may not have been exactly trimmed, and so the simulation was modified to obtain a periodic solution assuming a force imbalance corresponding to a particular "g" level of translational acceleration at the vehicle CG. Predictions were repeated for flight 423 with a small deceleration at the vehicle CG and small acceleration towards starboard (a_X =-0.015g, a_Y = 0.025 g), which shows much better agreement with test data in Fig. 16. The longitudinal accelerations predominantly affect pitch attitude predictions, whereas the roll attitude predictions are sensitive to lateral accelerations at the vehicle CG. When these accelerations were introduced into the trim process, no other quantities in the simulation predictions were altered significantly

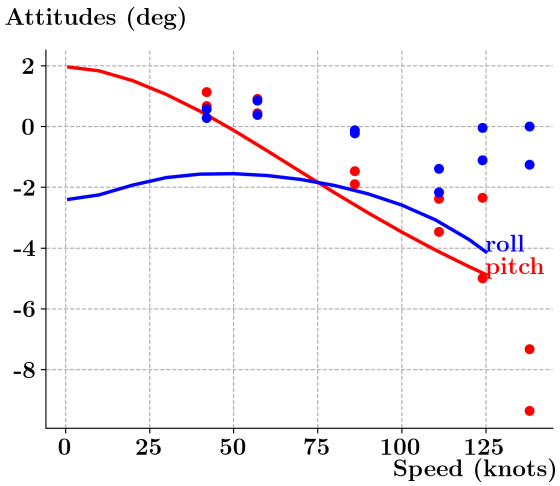

Fig. 15. Body Attitudes, Flight 423. (•: Test)

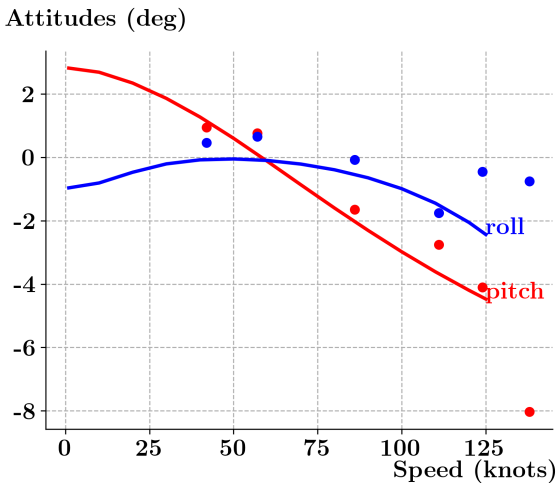

Fig. 16. Body Attitudes for small CG accelerations, Flight 423: a_X = -0.015g, a_Y = 0.025g (•: Test)

except for vehicle pitch and roll attitudes.

Figure 17 shows the variation of predicted and measured teeter angle cyclic 1/rev components with airspeed for flight 423. The longitudinal teeter (1c) component is well predicted up to 100 knots, while the lateral teeter angles exhibits a constant offset of +1.5 deg relative to the test data. The 1s teeter angle (lateral disk tilt) is negative, i.e. disk is tilted to the right, indicating that the CG may be offset towards port. Perturbations of assumed CG buttline station show that if the teeter predictions improve, then roll attitude and lateral control input correlations degrade. The discrepancy for this data set is currently unresolved.

Figure 18 shows the variation of blade coning angles (flap angles at blade root) with airspeed with only the first two blade modes, i.e. the fundamental flap and teetering modes. The prediction is generally good for the lateral and longitudinal disk tilt due to coning, i.e. the 1c and 1s components. The mean coning angle is nominally constant up to 80 knots, after which it decreases with airspeed. Predictions of coning angles with the elastic blade modes are shown in Fig. 19,

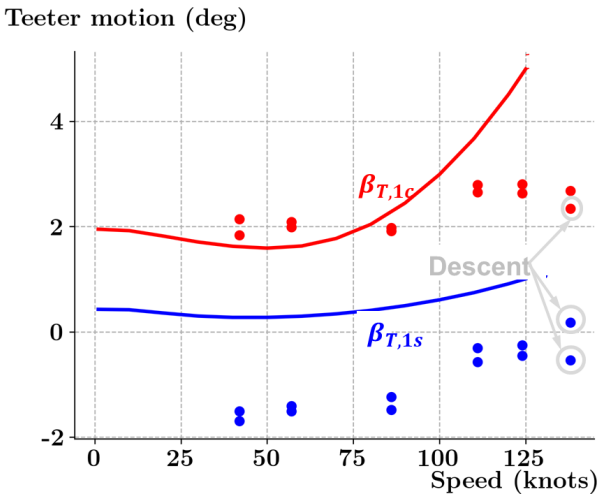

Fig. 17. Teeter Angles, Flight 423. (•: Test)

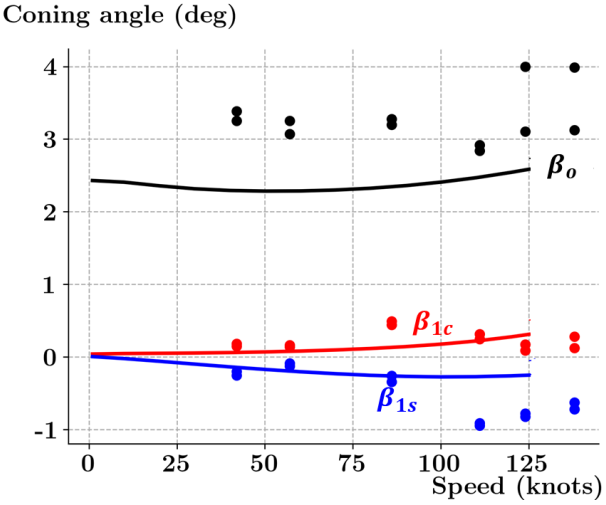

Fig. 18. Blade Coning Angles with only First Flap Modes, Flight 423. (•: Test)

which exhibit similar trends as flight 439, i.e. the average coning angle is nominally constant with airspeed, while the 1c and 1s components decrease slightly with airspeed. Overall, the time-varying component of the coning angle is minuscule (less than 0.5 deg) over the speed range investigated.

TEETER ANGLE STUDY

In this section, the rotor teeter angle β_T is studied under three conditions: (1) trimmed flight (2) small-accelerations with quasi-steady assumptions, and (3) unsteady maneuvers. Note that teeter clearances in trimmed flight are not necessarily related to the mast bumping phenomenon, but may provide insight into factors affecting blade teetering. The second type of flight condition is encountered when accelerations are small enough that the rotor motions can be considered approximately periodic over a short time period. Such an approach has been applied successfully for predicting the UH-60A rotor airloads (Ref. 16). In the final type of study, the vehicle is initially trimmed in forward flight and perturbation inputs are applied to the main rotor swashplate to study the response

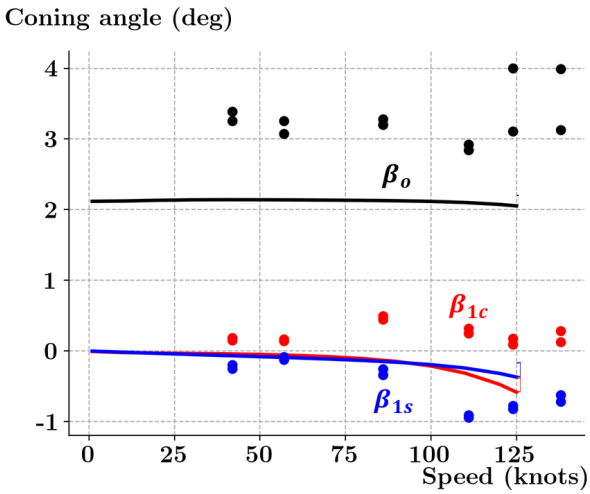

Fig. 19. Blade Coning Angles: Prediction with Elastic Modes, Flight 423. (•: Test)

time histories for both the vehicle body motions as well as the rotor blade teeter and flapping at the coning hinges, similar to the work in Ref. 10.

The R66 rotor head features an elastomeric teeter stop between the rotor head and rotor shaft. Owing to this design, two types of contact can occur between the rotor shaft and the teeter assembly: (1) a metal-to-elastomer contact at β_T = 7.4 deg (2) metal to metal contact at β_T = 15.1 deg. These two teeter angle limits will be referred to as Type-1 contact, and Type-2 contact respectively.

Trimmed Flight: Teeter Angle Analysis

At a nominal gross weight of 2200 lb, the teeter angles magnitudes are less than 6 degrees from 0 – 110 knots (Figs. 10 and 17). The predictions shows that placing the CG at the forward limit (9 inches ahead of main rotor shaft) has maximum aft teeter, i.e $\beta_T(1c)$ = - 6 deg at hover. As speed increases, the tip-path-plane is tilted to vector the rotor thrust forward and overcome fuselage drag; hence $\beta_T(1c)$ approaches zero as airspeed increases. The lateral teeter angle $\beta_T(1s)$ is near-constant at +2 deg over the speed range considered.

When the CG is at the aft limit, (2.5 inches behind the main rotor shaft), the hover prediction of aft teeter angle is $\beta_T(1c)$ = 2 deg, and the longitudinal teeter angle increases with airspeed to 3 deg at 100 knots. The lateral teeter angle $\beta_T(1s)$ is less than 1 degree. Therefore, placing the vehicle CG at the forward limit results in larger aft teeter in hover and lower teeter angles in forward flight, and vice versa when the CG is at the aft limit.

At lower gross weights, the vertical component of rotor thrust is lower but the horizontal component is the same for all weights, because fuselage drag is unchanged in cruise. The blade tip-path-plane must be tilted forwards more to preserve zero accelerations, resulting in larger teeter angles at lower weights.

The simulation model was trimmed at 3000 ft density altitude at both limits of the longitudinal CG locations (91 inch

and 102.5 inch). For the vehicle considered, the design max gross take-off weight is 2700 lb. The weight breakdown is as follows:

1. 1280 lb empty weight (fixed quantity)
2. Up to 500 lb fuel (variable)
3. Up to 5 passengers + baggage

A 1600 lb configuration with one 180-lb pilot, 100 lb/20% fuel and 40 lb baggage is chosen to study the teeter angles at a realistic lightweight condition. The predicted teeter angle Fourier coefficients and swashplate controls are shown in Figs. 20(a) and (b) respectively.

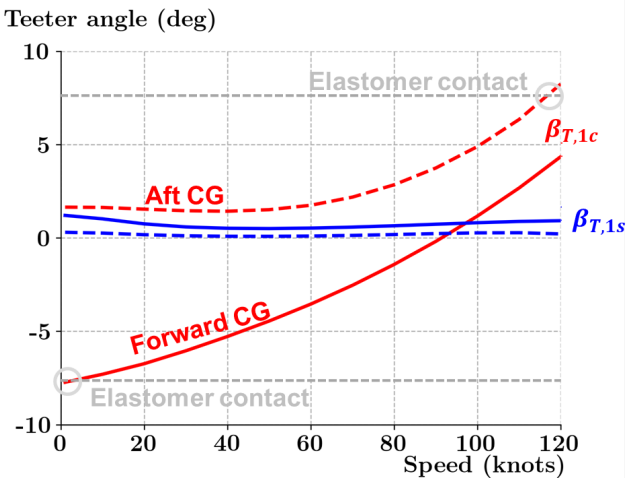

(a) Teeter Angles

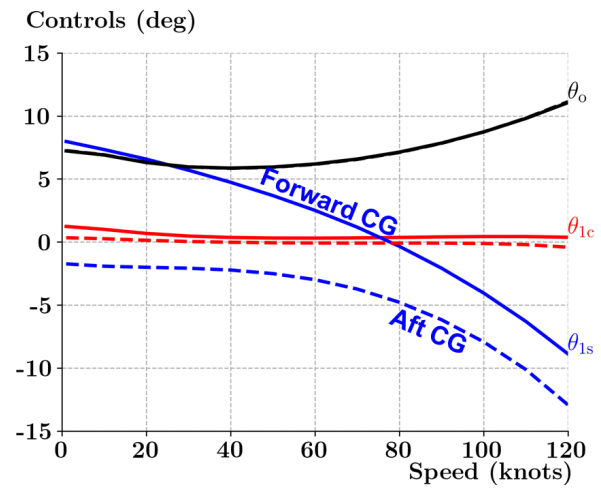

(b) Swashplate Controls

Fig. 20. Trim Results for Fore, Aft CG Limits

For the light configuration, the model predicts elastomer contact may occur in hovering flight when the CG is at the forward limit. For this weight and CG balance, the vehicle trims to a nose-down attitude and the tip-path-plane tilts back to align the line of action of rotor thrust with vehicle center of gravity. The trim longitudinal cyclic is short of its limiting value of 13.8 deg, and so it is possible to tilt the tip-path-plane further aft through pilot stick inputs. It has been shown (Appendix A) that this rotor configuration exhibits a one-to-one correspondence from cyclic feathering to teetering, thus more θ_{1s} would result in stronger Type-1 (elastomer) contact. The requirement to apply more aft stick input may arise while taking off and maneuvering (backwards) away from the landing site, or to overcome winds. Further, this teeter angle is unchanged by pitch-flap coupling in hover because teeter angles are ultimately driven by the need to align the tip-path-plane (which occurs due to teetering motions) and vector the rotor thrust for maneuvering the body. At 100 knots, the forward CG case exhibits near-zero lateral and longitudinal teetering, allowing for a significant margin before mast contact.

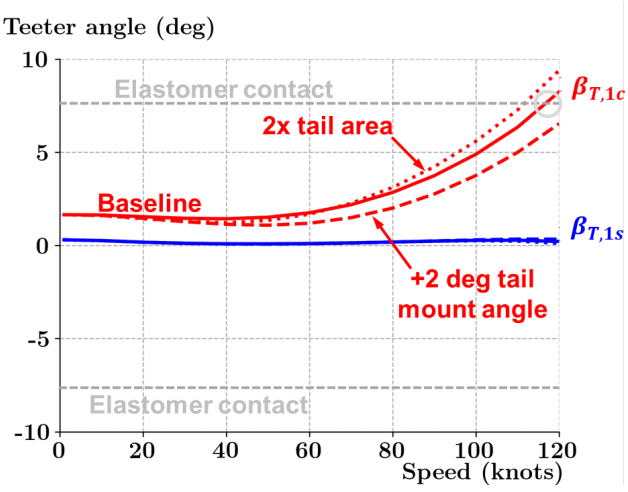

(a) Teeter Angles

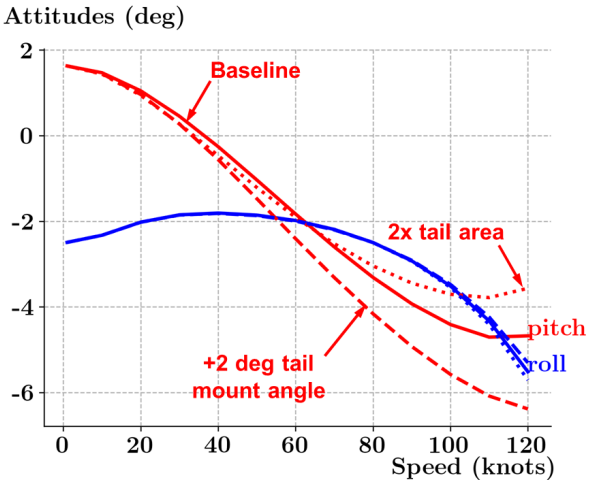

(b) Fuselage Attitudes

Fig. 21. Effect of Horizontal Tail Design: Aft CG Location

The aft CG limit is closer to the main rotor shaft than the forward CG limit, and so the hover condition exhibits very small stick input excursions and less than 3 degrees of teeter angle. At 100 knots, the maximum teeter angle is approximately 5 degrees of forward tilt, with 25% of additional longitudinal stick travel available for maneuvering. Increas-

ing the airspeed from 100 to 120 knots results in 44% more fuselage drag, and the corresponding increase in predicted teeter angle may result in Type-1 contact (the engine power required is a few hp above the MCP rating of 225 Hp for this lightweight configuration at 120 knots). Note, however, that the model over-predicts teeter angles in flight conditions above 100 knots and at aft CG and there is considerable uncertainty regarding this result. Additionally, Figure 20(b) shows that the longitudinal cyclic input is close to its limit, and so a stronger control-induced teeter stop contact may not occur at this flight condition. Select design perturbations are investigated to reduce the maximum teeter angle in cruise.

Design Perturbations: Horizontal Tail Parameters

In forward flight, teeter angles are coupled to body pitch angles and cyclic inputs through the longitudinal trim equations, i.e. vertical and horizontal force balance, and pitching moment balance. While it is not possible to change the drag or weight, it is possible to manipulate the horizontal tail lift through design, and correspondingly align the line of action of rotor thrust (i.e. normal to the tip-path-plane) closer to the rotor shaft. Horizontal tail lift can be increased (or decreased) by two means: (a) changing the horizontal tail mounting angle, or (b) changing the horizontal tail area. Both options were investigated for the aft CG case, and the corresponding teeter angle predictions as well as body attitudes are shown in Figs. 21 (a) and (b) respectively. Increasing the horizontal tail area to twice the baseline value increases the amount of elastomer contact, because the vehicle trims to a nose-down pitch attitude and the horizontal tail produces nose-up pitching moments about the CG. The tip-path-plane must tilt forward relative to the body to produce a counter-moment, resulting in increased teeter angles. A larger horizontal tail angle only reduces teeter stop clearances. However, increasing the tail mounting angle relative to the airframe by 2 degrees produces a more pronounced change for the aft CG case, because this design change alleviates the nose-down moment and forwarded tilt demanded of the main rotor, thus resulting in reduced teeter angle excursions even at 120 knots. For the forward CG case, the effect of changing the horizontal tail mounting angle also results in approximately 1 degree of additional nose-down body pitch attitude and a 1 degree reduced in the maximum teeter angles at 120 knots. Therefore, a larger horizontal tail mounting angle may help reduce the larger teeter angles predicted at higher speed level flight conditions with the "light" configuration. However, increasing the horizontal stabilizer angle reduces static longitudinal stability, possibly to the point of not meeting regulatory stability requirements.

Design parameters pertaining to rotor hinge offsets and pitch-flap coupling constants do not make a significant impact on the maximum teeter angles observed in level flight, because longitudinal moment balance drives the teeter angles.

Effect of Body Angular Velocity and Acceleration

The R66 simulation model was trimmed with various non-zero body angular rates and angular accelerations. Vehicle angular rates up to ± 60 deg/s and ± 60 deg/s^2 were investigated for in both pitch and roll axes. Body pitch rates and roll accelerations do not affect the teeter angles significantly. However, roll rates of 1 rad/s and pitch accelerations of 0.5 rad/s^2 cause inertial body pitching moments from Coriolis forces (associated with gyroscopic precession) and angular acceleration, respectively. This direct effect on longitudinal moment balance results in additional teeter angles to provide counter-moments from the main rotor of up to 1 degree at 120 knots. For more realistic values of pitch acceleration and roll rate, the changes in teeter angles are not significant.

Effect of Body Translational Accelerations

The R66 simulation model was trimmed with various non-zero translational accelerations. The effect of small lateral acceleration ($|a_y| \leq 0.1$g) on teeter angles is negligible. However, longitudinal and vertical accelerations have a noticeable effect on the teeter angles. Flying with -0.2g of additional vertical acceleration results in a 2 degree increase in teeter angle at 100 knots. Similarly, 0.1g of forward acceleration requires an additional 4 deg of forward disk tilt-, corresponding to 9 deg of maximum teeter angle. This effect may be reduced using a larger horizontal tail mounting angle.

Operation at Reduced RPM

In Ref. 10, a wind-tunnel simulation was carried out to identify if excessive flapping could occur at high thrust conditions and/or at high advance ratios. Excessive flapping was noted with reduced rotor RPM at $C_T/\sigma \geq 0.12$ for the R22 arising from retreating blade stall. However, this study assumed that the cyclics were "locked" and only collective travel was permitted, i.e. hub moments were not trimmed. For the R66 rotor, this blade loading corresponds to almost 3200 lb of rotor thrust at 90% RPM, and 3900 lb at 100% RPM, i.e., the vehicle would build up an enormous vertical rate of climb. In a realistic scenario, a helicopter is flown with more nominal accelerations, and with more attention paid to the hub moments. Numerical simulations were carried out to verify that at higher take-off weights (or vertical load factors), the teeter angles *decrease* for the R66 rotor, instead of increasing even at 90% of the design rotor speed. Two possible reasons for the differences in findings between these two studies are (1) the R22 has 8 deg of nose-down blade twist, whereas the R66 blade features a nominal 4 deg of nose-down rotor blade twist. An untwisted blade can carry more lift at higher advance ratios (with zero lateral lift offset) without suffering from negative lift at advancing blade tips; (2) application of longitudinal cyclic to trim out the hub pitching moments reduces the aft tip-path-plane tilt that arises from lift imbalance between the advancing and retreating sides of the rotor disk.

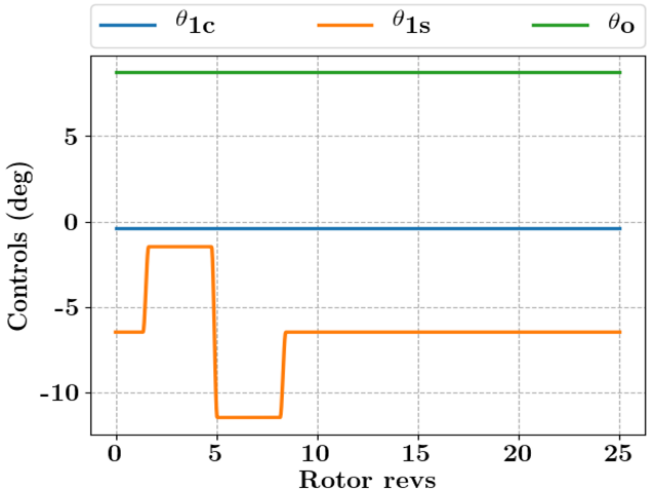

(a) Control Inputs

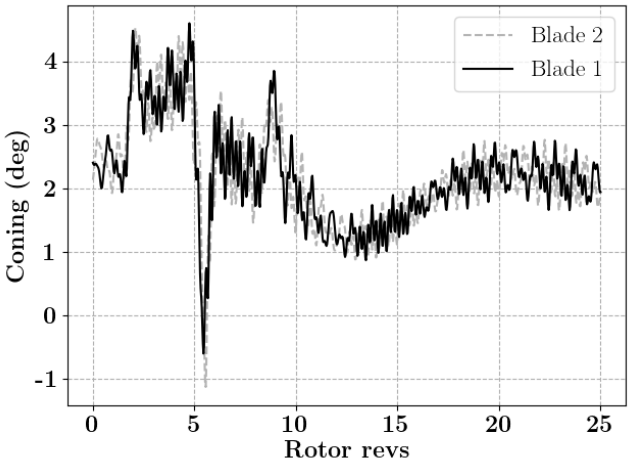

(b) Coning Angles

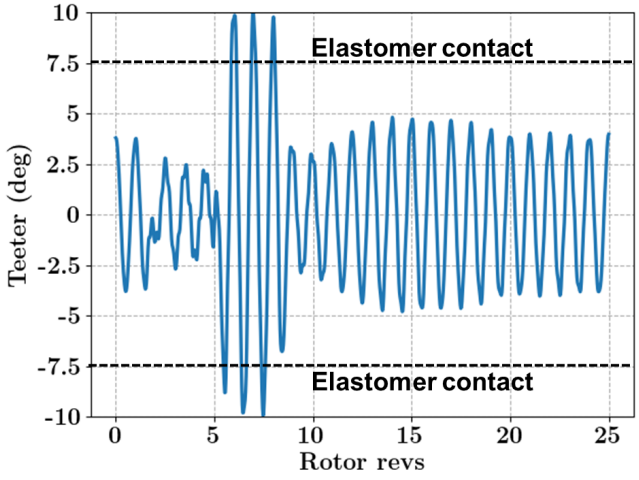

(c) Teeter Angle

Fig. 22. Pull-up/Push-over Simulation at 100 knots with Baseline Design

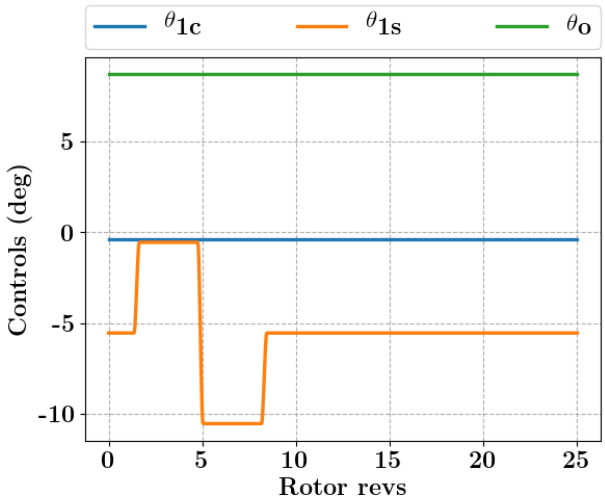

(a) Control Inputs

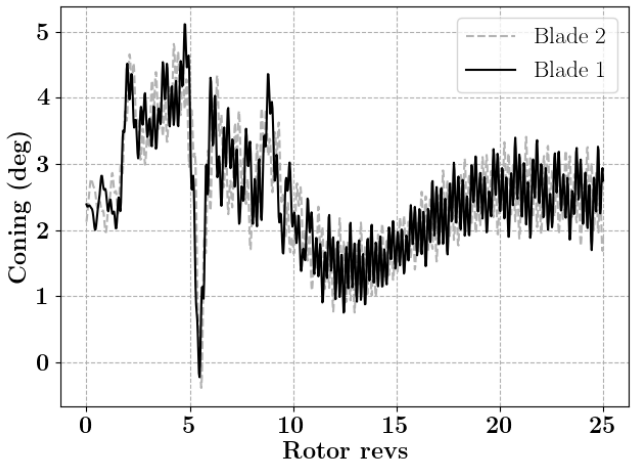

(b) Coning Angles

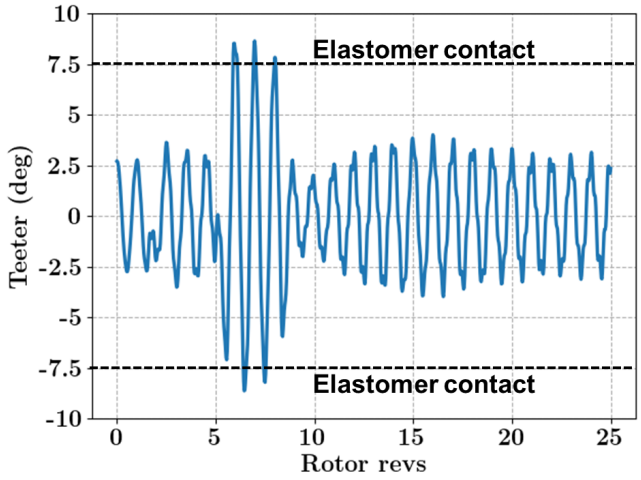

(c) Teeter Angle

Fig. 23. Pull-up/Push-over Simulation with +2 deg Horizontal Tail Mounting Angle

Under normal operating conditions, the R66 rotor does not seem to be susceptible to excessive stall-induced teetering at high thrust conditions - the teeter angles are lower at higher thrust conditions in trimmed flight.

Time Marching Analysis

In this section, a 2200-lb vehicle with aft CG (2.5 inches behind the main rotor) is initially trimmed in steady forward flight and subsequently, a doublet input in the longitudinal cyclic is applied, i.e., $-\Delta\theta_{1s}$ is applied to initiate a pull-up, followed by forward correction $+2\Delta\theta_{1s}$, and finally the stick position is returned to the trim setting. Lateral cyclic is held fixed in the initial trimmed position. While this is unlikely to be representative of the control inputs that lead to mast bumping, this represents a maneuver that is convenient for comparative studies. A mast bump may include a lateral cyclic component as the pilot reacts to unanticipated body attitude changes occurring in conjunction with the low-g condition.

A time marching simulation with the control inputs described as above was performed with $\Delta\theta_{1s} = 5$ deg and a maneuver duration of 1 second. The time histories of main rotor swashplate controls are shown in Fig. 22(a). Between 1.5 and 5 rotor revolutions, the aft stick input results in backward tilt of the tip-path-plane and increase in rotor thrust, reflected by a corresponding increase in the blade coning angles shown in Fig. 22(b). The corresponding teeter angle time histories are shown in Fig. 22(c). At trim, the teeter angle magnitude is 2.75 deg. Upon application of aft stick (nose up blade pitch on advancing side), the maximum teeter angle decreases slightly to 2.5 degrees. When forward stick is applied (nose down blade pitch on advancing side), the tip-path-plane tilts forward due to additional teetering motion. The maximum teeter angle increases to 10 degrees, representing a significant Type-1 contact with the elastomeric stop. When the cyclic pitch is returned to its neutral position, the teeter angle amplitudes return to 2.75 degrees. However, the brief but noticeable contact enables us to establish a baseline case for comparison purposes, and perturb design parameters to reduce the severity of this contact, or eliminate it entirely.

The model also shows that low thrust (indicated by the blade coning angles) is not an exclusive indicator of mast contact with the rotor head. Between 5 and 8 rotor revolutions, the rotor thrust initially decreases upon removal of aft stick input, and continues to decrease with the rate of change of stick input. Once the control input is held fixed at -12 deg, the coning angle recovers its nominal value of 2.4 deg while the teeter angle continues to oscillate and making Type-1 elastomer contact. It should be noted that the negative coning angles represent contact between the blades and their droop stops.

The simulation was repeated with the horizontal tail pitch angle increased by 2 degrees, and the time history of the teeter angle is shown in Fig. 23. An analysis of the results shows that with 2 deg more of horizontal tail mounting angle, the trim position of the longitudinal cyclic is -5.54 deg vs. -6.5 deg. The maximum teeter angles in trim for the two cases are 2.5 deg (larger tail angle) and 2.75 deg for the baseline.

For the same perturbation stick inputs relative to the trim setting, however, the model shows the design with the larger tail incidence exhibits significantly lower elastomer contact (maximum teeter angle of only 8.3 deg) compared to the baseline design (10 deg). This finding is consistent with the steady flight analysis carried out in previous sections. If the trim value of the maximum teeter angle is small, the design allows for larger cyclic inputs to be applied and affords more maneuverability before the rotor head contacts the mast. Once again, however, it should be noted that these improved clearances are not necessarily indicative of an improvement in resistance to mast bumping.

Effect of Other Design Parameters

The time marching study was repeated for different values of rotor speed (90% and 110%), blade chord, pitch-flap coupling constants, and rotor hub waterline location. The effects of changing each of the design parameters are listed below:

1. Decreasing the **rotor radius** by 2 ft reduces the maximum teeter angle observed during the maneuver from 10 deg to 8 deg. However, this design parameter will have significant repercussions on the design of other helicopter components, and may be impractical.

2. Increasing **rotor speed** to 110% of the baseline does not reduce the maximum teeter angles. However, decreasing the rotor speed to 90% of the baseline value reduces the maximum teeter angle from 10 deg to 8.8 deg. As in the case of rotor radius change, rotor speed change also involves a major redesign of several airframe components as well as the main rotor blade to avoid resonance. At 90% RPM, the third anti-symmetric flap and first torsion modes are close to resonance.

3. The **rotor shaft mounting angle** in the airframe is 0 deg for the baseline design. When the shaft is mounted with a forward tilt of 2.5 deg, the maximum teeter angle excursions (even for the large control perturbations considered) are well within the Type-1 contact limit with an aft CG configuration, as shown in Fig. 24. When the main rotor shaft is mounted with a forward tilt, additional teetering is not required to align the rotor thrust forwards to counteract airframe drag. The disadvantage of this design change is that when the CG fuselage station is at the fore limit (9 inches ahead of the main rotor), then the teeter angles at hover exceed the design limit. One possible work-around is to reduce the allowable CG travel and/or move the main rotor hub forwards, which again is unlikely to be practical.

4. If aggressive streamlining measures are used to reduce **fuselage parasitic drag** from 7.5 sq.ft to 6.0 sq.ft, the maximum teeter angle reduces from 10 deg to 9 deg. However, it may not always be possible to reduce drag

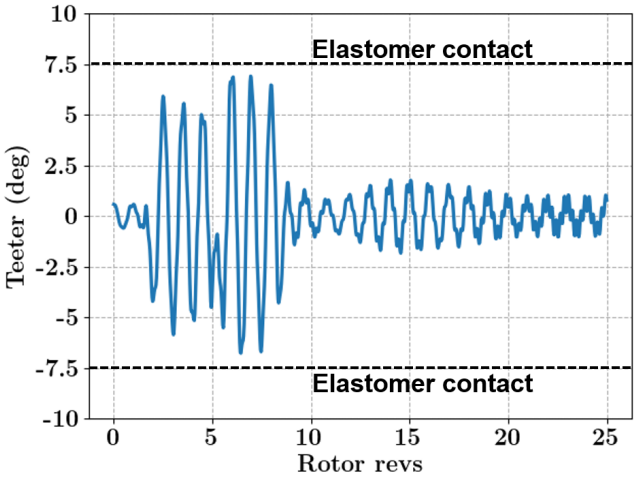

Fig. 24. Teeter angles for Pull-up/Push-over Maneuver with 2.5 deg forward shaft tilt; CG at aft limit

for all configurations, e.g. if camera equipment needs to be externally mounted.

5. Increasing **blade chord** by 20% does not alter the maximum teeter angles observed. Decreasing blade chord by 20% decreases the maximum teeter angle from 10 deg to 9.5 deg.

6. Moving the pitch link closer to the blade pitching axis amplifies the **pitch-flap coupling**, but does not reduce the maximum teeter angles. Similarly, decreasing both pitch-teeter and pitching coning couplings does not alleviate the larger teeter angles observed for the control inputs applied.

7. Changing the **main rotor hub waterline station** 10 inches above or below the baseline design value does not affect the maximum teeter angle observed when forward stick is applied.

8. Modifying the **vertical offset between the teeter hinge and coning hinges** does not significantly alter the maximum teeter angles observed during the maneuver.

9. Decreasing the **main rotor blade twist** from -4 deg to an untwisted design results in incrementally lower teeter angles (10 deg to 9.5 deg), while increasing the twist to -6 deg does not significantly alter the maximum teeter angles.

10. **Blade airfoil design** (10% lower drag, 10% more lift or zero pitching moments) does not affect the quantitative values of the teeter angles observed.

CONCLUSIONS AND FUTURE WORK

A simulation model of a teetering rotor tri-hinge design was formulated and partially validated against test data for the R66 helicopter. The model was used to study the teeter angle characteristics of the vehicle in forward flight when subject to longitudinal stick inputs.

1. The use of the tri-hinge design results in reduced loads at both the blade root, as well as reduced bending loads in the rotor mast. The unique feature of this design is that in steady flight, the flap angle at the outboard "coning" hinge is nominally constant, and tip-path-plane tilt is achieved through cyclic tilt of the rotor system about the teeter hinge.

2. The elastic flap modes of a teetering rotor occur in pairs, with one anti-symmetric and one symmetric mode. In the anti-symmetric modes, the teeter hinge rotation degree of freedom participates and both blades have equal and opposite root flap angles. In the symmetric modes, the teeter hinge behaves as if it is locked, and the mode shapes are those of an articulated rotor.

3. The nonlinear dual delta-3 couplings can be approximated as two linear relationships between the (destabilizing) pitch-coning feedback and the (stabilizing) pitch-teeter feedback. For the R66 rotor, the equivalent delta-3 angles are +12.95 deg and -18.4 deg, respectively, for the pitch-coning and pitch-teeter couplings.

4. Modeling the phase angle difference between the blade and swashplate inputs using the kinematics of the control system is essential in obtaining good control angle predictions, especially for the lateral cyclic θ_{1c}. The 18 deg phase lag is advantageous because this design allows for the lateral stick input to remain nominally constant with airspeed up to 120 knots.

5. The model was used to predict hub clearances for trimmed flight, quasi-steady accelerated flight and an unsteady maneuver to study the effects of varying design parameters. Of the parameters investigated, only changing the horizontal tail mounting angle on the airframe was found to be effective in reducing the maximum teeter angle. However, increasing the horizontal tail angle will have an adverse effect on static stability, and all relevant ramifications of this design change must be taken into account, necessitating further analysis.

The results presented in this paper are representative of preliminary results from an ongoing research effort, and are subject to significant uncertainty owing to the various simplifying assumptions in modeling the coupled rotor and body flight dynamics. Prior to drawing conclusions about the vehicle design, the analysis must be further refined and validated, and the scope of the simulations must be expanded. Also necessary is additional investigation of the flight conditions leading to mast bumping to ensure that the parametric design studies provide a valid prediction of improvements in resistance to mast bumping.

Confidence in the results will be improved with improvements in predictions of trim conditions (especially for the aft CG location) and additional validation of the model in unsteady flight with maneuver data from tests.

REFERENCES

[1]Shamie, J. and Friedmann, P., "Aeroelastic Stability of Complete Rotors with Application to a Teetering Rotor in Forward Flight," *Journal of Sound and Vibration*, Vol. 53, (4), 1977, pp. 559–584.

[2]Yeo, H. and Chopra, I., "Coupled Rotor/Fuselage Vibration Analysis for Teetering Rotor and Test Data Comparison," *Journal of Aircraft*, Vol. 38, (1), Aug 2001, pp. 111–121.

[3]Floros, M. W. and Johnson, W., "Stability and Control Analysis of the Slowed-Rotor Compound Helicopter Configuration," *Journal of the American Helicopter Society*, Vol. 52, (3), 2007, pp. 239–253.

[4]Rezgui, R., Lowenberg, M., and Bunniss, P., "Experimental and Numerical Analysis of the Stability of an Autogyro Teetering Rotor," 64^{th} Annual Forum of the American Helicopter Society International, Montreal, Canada, April 29–May 1, 2008.

[5]Avanzini, G., Matteis, G., Lucertini, F., and Torasso, A., "Dynamic Behaviour and Response of a Two-bladed Gimballed Rotor," 36^{th} European Rotorcraft Forum, Paris, France, Sep 7–9, 2010.

[6]Shen, J., Masarati, P., Bain, J., and Hodges, T., "Multibody Dynamics Model of a VTOL Teetering Rotor," American Helicopter Society Aeromechanics Specialist's Conference, San Francisco, CA, Jan 20–22, 2010.

[7]Drees, J., Sonneborn, W., and Yen, J., "Hub spring Moment Isolation in Underslung Two-bladed Teetering Rotor," US Patent 4,115,031, September 19 1978.

[8]Dooley, L. and Ferguson, S. I., "Effect of Operational Envelope Limits on Teetering Rotor Flapping," Technical report, USARTL TR 78-9, July 1978.

[9]Dooley, L., "Rotor Blade Flapping Criteria Investigation," Technical report, USAAMRDL TR 76-33, December 1976.

[10]Sarathy, S., Schrage, D., and Losier, P., "An Investigation of Excessive Blade Flapping in the Robinson R22 Helicopter," 53^{rd} Annual Forum of the American Helicopter Society, 1997.

[11]Rubenstein, G., Moy, D. M., Sridharan, A., and Chopra, I., "A Python-based Framework for Real-time Simulation Using Comprehensive Analysis," 72^{nd} Annual Forum of the American Helicopter Society, West Palm Beach, FL, May 16–18, 2016.

[12]Govindarajan, B. M. and Leishman, J. G., "Predictions of Rotor and Rotor/Airframe Configurational Effects on Brownout Dust Clouds," *Journal of Aircraft*, Aug 2015, pp. 1–16.

[13]Peters, D. A., and He, C., "Comparison of Measured Induced Velocities with Results from a Closed-Form Finite State Wake Model in Forward Flight," Proceedings of the 45th Annual Forum of the American Helicopter Society, Boston, MA, May 22–24, 1989.

[14]Passe, B., Sridharan, A., and Baeder, J. D., "Computational Investigation of Coaxial Rotor Interactional Aerodynamics in Steady Forward Flight," 33^{rd} AIAA Applied Aerodynamics Conference, Dallas, TX, June 22–26, 2015.

[15]Brenan, K., Campbell, S., Campbell, S., and Petzold, L., *Numerical Solution of Initial-Value Problems in Differential-Algebraic Equations*, Classics in Applied Mathematics, Society for Industrial and Applied Mathematics, 1989.

[16]Bhagwat, M. J., Ormiston, R. A., Saberi, H. A., and Xin, H., "Application of computational fluid dynamics/computational structural dynamics coupling for analysis of rotorcraft airloads and blade loads in maneuvering flight," *Journal of the American Helicopter Society*, Vol. 57, (3), 2012, pp. 1–21.

APPENDICES

A: Simplified Tri-Hinge Flap Dynamics Model

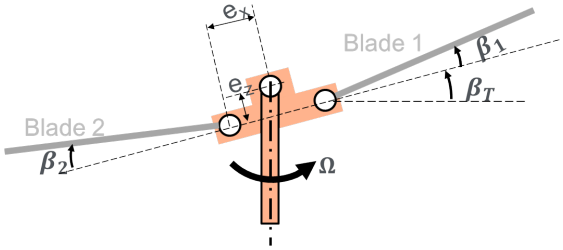

Fig. 25. Tri-hinge 3-DOF model

Consider a tri-hinge teetering rotor hub as shown in Fig. 25. The governing equations of the tri-hinge system in vacuum for a steady flight condition are given by

$$I_\beta(\beta_1^{**}+\nu_\beta^2\beta_1)+(I_\beta+e_xS_\beta)[\beta_{\mathrm{T}}^{**}+\beta_{\mathrm{T}}] \;=\; \frac{1}{\Omega^2}M_{\beta 1}$$

$$I_\beta(\beta_2^{**}+\nu_\beta^2\beta_2)-(I_\beta+e_xS_\beta)[\beta_{\mathrm{T}}^{**}+\beta_{\mathrm{T}}] \;=\; \frac{1}{\Omega^2}M_{\beta 2}$$

$$2(I_b+e_z^2M_b)\beta_{\mathrm{T}}^{**} \;+\; 2(I_b-e_z^2M_b)\beta_T \;+\; (I_\beta+e_xS_\beta)[\beta_1^{**}-\beta_2^{**} \;+\; \beta_1-\beta_2] \;=\; \frac{1}{\Omega^2}M_T$$

The coefficients of flap inertia I_β, S_β retain their usual meanings. I_b refers to the inertia of the blade about the teeter hinge and M_b is the total blade mass. $M_{\beta 1}$ and $M_{\beta 2}$ are the flap moments due to aerodynamic loads at the individual blade coning hinges, while M_T is the total aerodynamic flap moment at the teeter hinge. Expressing the dynamics in fixed-frame coordinates allows for simplification of the governing equations as follows.

The collective flapping equation (about the coning hinges) is given by

$$B_o^{**} + \nu_\beta^2 B_o = \frac{\gamma}{8}\overline{M}_{B_o} \quad (10)$$

The collective flapping degree of freedom is given by

$$B_o = \frac{1}{2}(\beta_1 + \beta_2)$$

The differential flapping equation (about the coning hinges) is given by

$$B_d^{**} + \nu_\beta^2 (B_d + \beta_T^{**} + \beta_T) = \frac{\gamma}{8}\overline{M}_{B_d} \quad (11)$$

The differential flapping degree of freedom is given by

$$B_\mathrm{d} = \frac{1}{2}(\beta_1 - \beta_2)$$

The teetering mode equation is

$$K_1(B_d^{**} + B_d) + \beta_T^{**} + \nu_T^2 \beta_T = \frac{\gamma}{8}\overline{M}_T \quad (12)$$

Where K_1 is the ratio of flap inertia to teeter inertia, given by

$$K_1 = \frac{I_\beta + e_x S_\beta}{I_b + e_z^2 M_b}$$

ν_T represents teeter natural frequency, and is given by

$$\nu_\mathrm{T} = \sqrt{\frac{I_b + e_z^2 M_b}{I_b - e_z^2 M_b}} \approx 1 - \frac{M_b e_z^2}{I_b}$$

The collective flapping mode (coning mode) is uncoupled from the teetering and differential modes, and has a natural frequency of ν_β/rev. The coupled teeter-differential flapping modes have two frequencies. The teeter frequency is very close to 1/rev, while coupled differential flapping/teetering has a much higher natural frequency (5/rev). The simple analysis reveals that significant differential flapping is excited only by higher harmonic loading (upwards of 3/rev). At lower frequencies, any differential lift results in teetering motions. The vertical offset between the teeter hinge and coning hinges introduces a small 1/rev flapping response at the coning hinge. Without this vertical offset, the 1/rev tip-path-plane tilt originates entirely from teetering motions.

In hover, the aerodynamic loads are analytically examined assuming a linear airfoil lift-curve slope, uniform inflow and fixed controls. The steady coning angle is

$$B_o = \frac{\gamma}{8\nu_\beta^2}\left[\theta_o\left(1 - \frac{4e_x}{3R}\right) - \lambda\left(\frac{4}{3} - \frac{2e_x}{R}\right)\right] \quad (13)$$

Differential flapping vanishes in hover, while the teeter angle harmonics are

$$\beta_{\mathrm{T,1c}} = -\theta_{1s}$$
$$\beta_{\mathrm{T,1s}} = \theta_{1c}$$

Thus, tip-path plane tilt is achieved exclusively through blade teetering motions, while coning occurs mainly due to steady (mean) forcing.

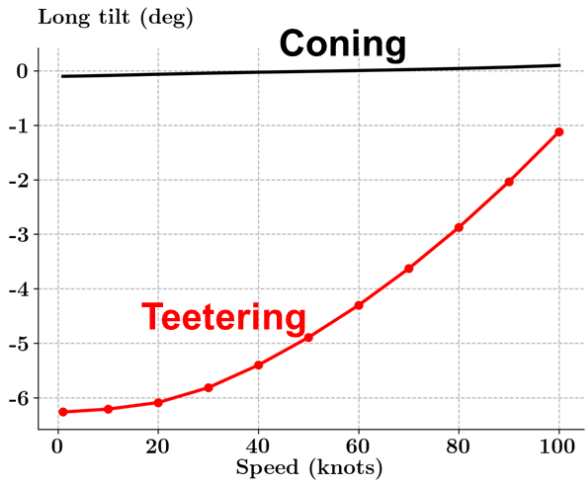

Fig. 26. Longitudinal tip-path-plane tilt: contributions

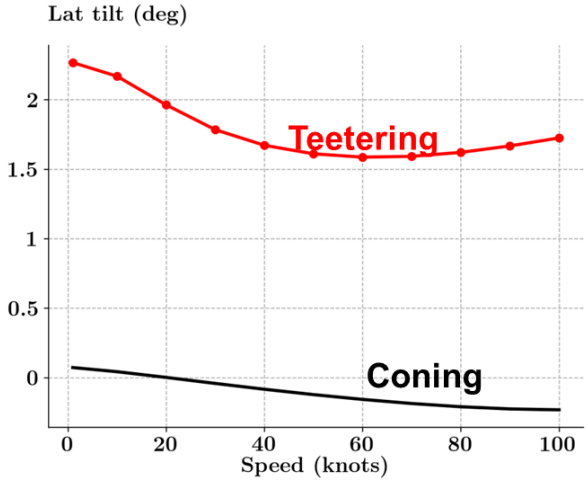

Fig. 27. Lateral tip-path-plane tilt: contributions

It is difficult to obtain similarly straightforward analytical expressions for the blade response in forward flight. Instead, a numerical simulation was performed with the comprehensive analysis to compare the quantitative values of cyclic flapping due to teetering vs. blade motions. Figures 26 and 27 show the variation of 1/rev longitudinal and lateral flapping (with airspeed) due to cyclic flapping at the coning hinges, and at the teeter hinge. Over the range of flight conditions considered, 1/rev blade flapping due to teeter motions is more than 10× the contribution from individual blade flapping ("coning").

B: Pitch-Flap Coupling

The delta-3 relationship between blade flapping/teetering and pitch change is inherently nonlinear, and modeled exactly using kinematics of the pitch link and its attachment to both the

blade and the rotating swashplate. This geometry is modeled independently of the coupled rotor/body dynamics and studied to identify a simplified representation for integration into the comprehensive analysis. The swashplate analysis can calculate the blade root pitch setting for a given swashplate travel (collective and two cyclics), teeter angle β_T and coning angle β_1, β_2.

To identify the delta-3 coefficients, the swashplate cyclics inputs were set to their neutral points so as to provide constant blade pitch over the entire azimuth. Three separate studies were conducted to identify the effect of coning (in the absence of teeter), effect of teeter (in the effect of coning) and the effect of simultaneous coning and teeter.

Effect of Coning Only For this study, the blade teeter angles were set to zero, and the coning angle was increased over a range of 5 degrees. The swashplate collective pitch setting was increased from 0% to 100% travel, and the resulting pitch angle was obtained from the kinematic analysis. The variation of blade pitch angle with collective setting for various coning angles is shown in Fig. 28. As coning increases, the pitch angle increases due to the destabilizing delta-3 feedback.

The slope of pitch setting to the coning angle (i.e. delta-3 coefficient) was also extracted numerically from the data and is shown for various collective settings in Fig. 28. The slope $\frac{\Delta\theta}{\Delta\beta_o}$ is almost constant across the entire collective range, and corresponds to a delta-3 angle of +12.93 deg.

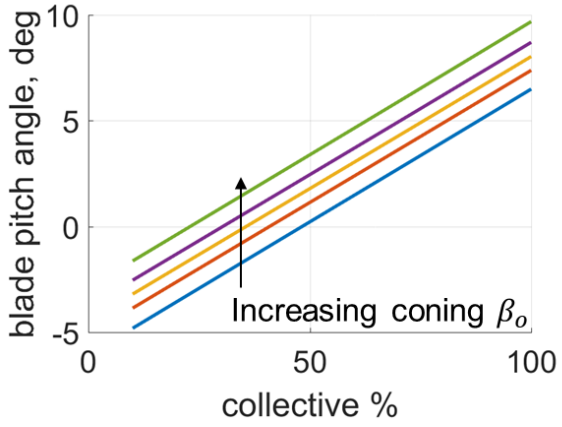

Fig. 28. Effect of coning angle β_o on blade pitch θ

Effect of Teeter Only For this study, the blade coning angles were set to zero, and the teeter angle was varied from -7 to +7 degrees. The swashplate collective pitch setting was increased from 0% to 100% travel, and the resulting pitch angle was obtained from the kinematic analysis. The variation of blade 1 pitch angle with collective setting for various teeter angles is shown in Fig. 30. As teeter increases, the pitch angle decreases due to the stabilizing delta-3 feedback.

The slope of the blade pitch angle to teeter angle coupling (i.e. delta-3 coefficient) was also extracted numerically from the data and is shown for various collective settings in Fig. 31.

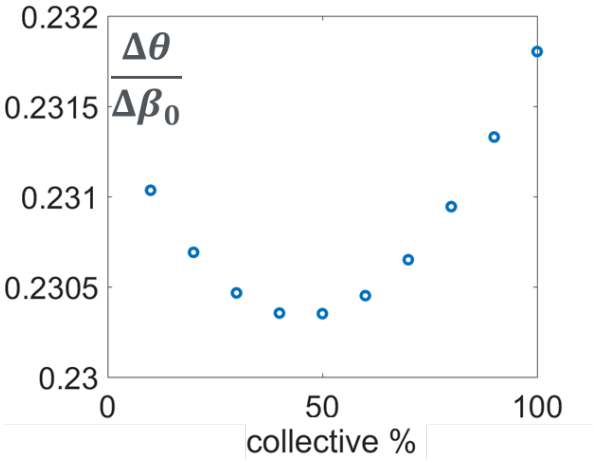

Fig. 29. Variation of pitch-to-coning delta-3 coefficient $K_{P_{\beta_o}}$ with collective input δ_o

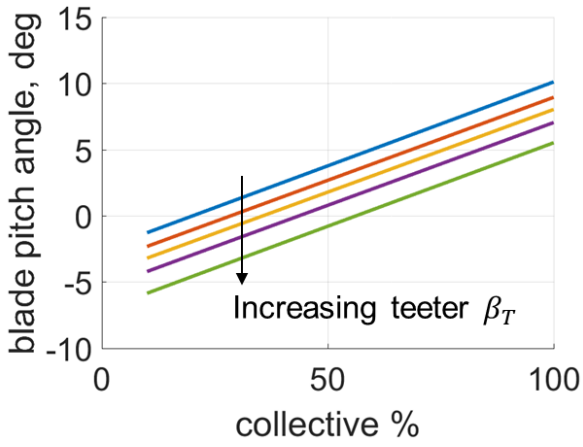

Fig. 30. Effect of teeter β_T on blade pitch θ

The slope $\frac{\Delta\theta}{\Delta\beta_T}$ is almost constant across the entire collective range, and corresponds to a delta-3 angle of -18.4 deg.

Effect of Teeter + Coning For this study, the blade coning angles and teeter angles were varied simultaneously as the collective input δ_o was increased from 0% to 100% travel. The resulting pitch angle was obtained from the kinematic analysis and processed to study the linear and nonlinear dependencies of pitch on teeter and coning blade motions.

As in the previous two studies, blade pitch is perfectly linear with collective input for fixed teeter and coning angles. Therefore, the slope of this line, i.e. $\frac{\Delta\theta}{\Delta\delta_o}$ can be analyzed to identify any dependence on blade motions. Figure 32 shows the variation of this slope $\frac{\Delta\theta}{\Delta\delta_o}$ with the coning angle β_o for various teeter angles (each line is a different teeter angle). The data exhibits only a weak dependence on both coning and teeter angles, and the slope of pitch to collective input is fairly constant over all blade motions of interest. Similar trends were obtained for the cyclic inputs $\delta_{\text{lat}}, \delta_{\text{lon}}$ and their corresponding outputs. Therefore, pilot control sensitivity is not significantly affected by the delta-3 mechanisms for this

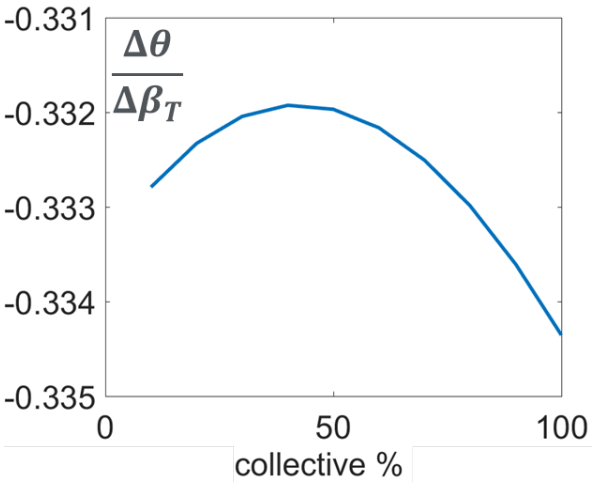

Fig. 31. Variation of pitch-to-teeter delta-3 coefficient $K_{P_{\beta_T}}$ with collective input δ_o

system, and can be considered independent of delta-3 induced pitch changes.

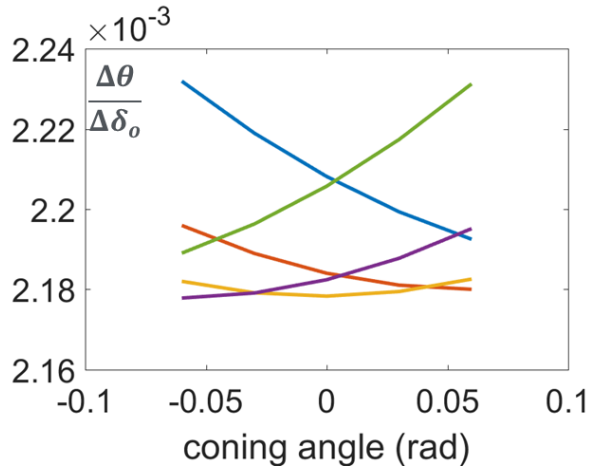

Fig. 32. Variation of θ-δ_o slope with coning β_o for various teeter angles

The intercept of the θ-δ_o line contains the effect of delta-3 coupling, and is analyzed further for insight into the nature of the pitch-flap and pitch-teeter feedback. Curve fits of the data show that the delta-3 induced pitch change can be expressed in the following form:

$$\theta(\beta_T, \beta_o) = K_{p_{\beta_T}}\beta_T + K_{p_{\beta_o}}\beta_o + c_1\beta_T\beta_o + c_2\beta_T^2\beta_o \quad (14)$$

The coefficients $K_{P_{\beta_T}}$ and $K_{P_{\beta_o}}$ are not constant for all teeter and coning angles, but vary less than 1% for the operating range of blade motions and swashplate travel considered. Further, the coefficients of the higher-order terms (c_1, c_2) are such that the nonlinear effects contribute less than 0.1 deg to total blade pitch angles, and can be ignored. Therefore, the delta-3 induced pitch angle for the two blades is approximated to

$$\begin{aligned}\theta_1(\beta_T, \beta_1) &= -0.332\beta_T + 0.23\beta_o \\ \theta_2(\beta_T, \beta_2) &= 0.332\beta_T + 0.23\beta_o\end{aligned}$$

Appendix C

The first 3 modes for the teetering rotor system are shown, in order, in Figs. 33(a) – (f).

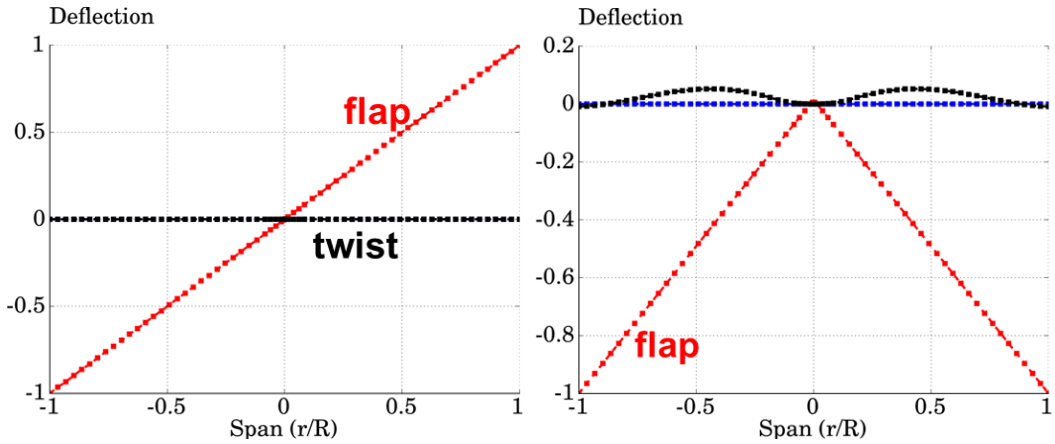

(a) Mode 1: Teeter (A, 0.99/rev)

(b) Mode 2: Coning (S, 1.01/rev)

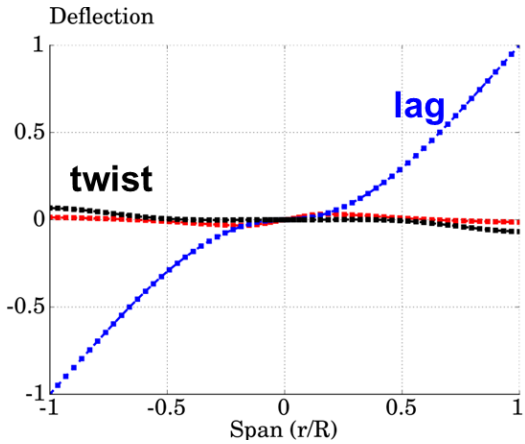

(c) Mode 3: 1st lag (A, 1.5/rev)

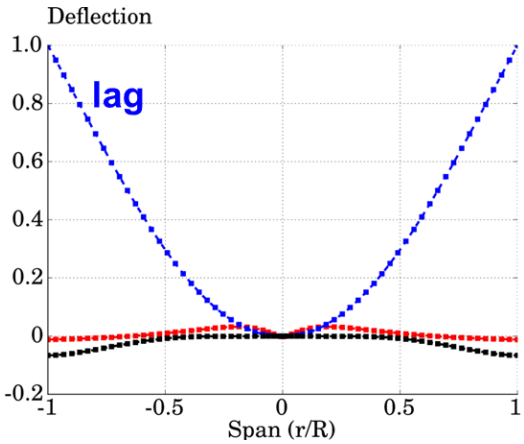

(d) Mode 4: 1st lag (S, 1.5/rev)

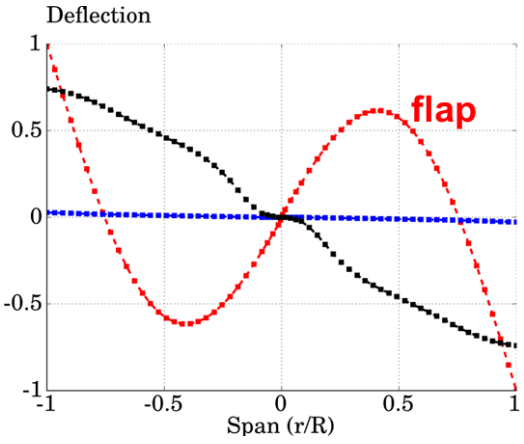

(e) Mode 5: 2nd flap (A, 2.69/rev)

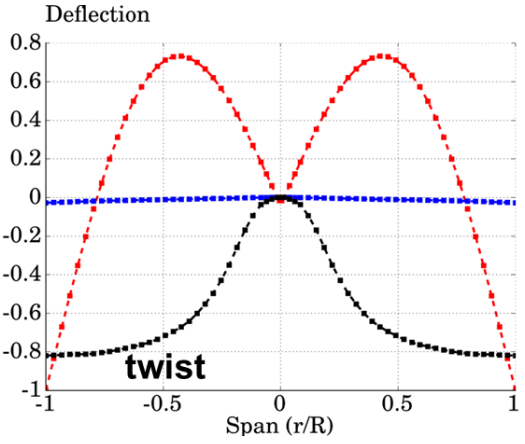

(f) Mode 6: 2nd flap (S, 2.75/rev)

Fig. 33. Elastic beam modes for teetering rotor